AGU PUBLICATIONS

JGR

Journal of Geophysical Research: Oceans

RESEARCH ARTICLE

10.1002/2014JC010598

A three-dimensional map of tidal dissipation over abyssal hills

Adrien Lefauve[1,2], Caroline Muller[3], and Angélique Melet[4]

[1]Laboratoire d'Hydrodynamique de l'École Polytechnique, Palaiseau, France, [2]Now at Department of Applied Mathematics and Theoretical Physics, Centre for Mathematical Sciences, University of Cambridge, Cambridge, UK, [3]CNRS/Laboratoire d'Hydrodynamique de l'École Polytechnique, Palaiseau, France, [4]CNES/Laboratoire d'Études en Géophysique et Océanographie Spatiales, Toulouse, France

Key Points:
- First 3-D global map of tidal dissipation above small-scale abyssal hills derived
- Spatial inhomogeneity of tidal mixing suggested could affect ocean circulation
- Implications for parameterizations of tidal mixing in ocean models are discussed

Supporting Information:
- Supporting Information S1

Correspondence to:
A. Lefauve,
lefauve@damtp.cam.ac.uk

Citation:
Lefauve, A., C. Muller, and A. Melet (2015), A three-dimensional map of tidal dissipation over abyssal hills, *J. Geophys. Res. Oceans*, *120*, doi:10.1002/2014JC010598.

Received 19 NOV 2014
Accepted 3 JUN 2015
Accepted article online 8 JUN 2015

Abstract The breaking of internal tides is believed to provide a large part of the power needed to mix the abyssal ocean and sustain the meridional overturning circulation. Both the fraction of internal tide energy that is dissipated locally and the resulting vertical mixing distribution are crucial for the ocean state, but remain poorly quantified. Here we present a first worldwide estimate of mixing due to internal tides generated at small-scale abyssal hills. Our estimate is based on linear wave theory, a nonlinear parameterization for wave breaking and uses quasi-global small-scale abyssal hill bathymetry, stratification, and tidal data. We show that a large fraction of abyssal-hill generated internal tide energy is locally dissipated over mid-ocean ridges in the Southern Hemisphere. Significant dissipation occurs above ridge crests, and, upon rescaling by the local stratification, follows a monotonic exponential decay with height off the bottom, with a nonuniform decay scale. We however show that a substantial part of the dissipation occurs over the smoother flanks of mid-ocean ridges, and exhibits a middepth maximum due to the interplay of wave amplitude with stratification. We link the three-dimensional map of dissipation to abyssal hills characteristics, ocean stratification, and tidal forcing, and discuss its potential implementation in time-evolving parameterizations for global climate models. Current tidal parameterizations only account for waves generated at large-scale satellite-resolved bathymetry. Our results suggest that the presence of small-scale, mostly unresolved abyssal hills could significantly enhance the spatial inhomogeneity of tidal mixing, particularly above mid-ocean ridges in the Southern Hemisphere.

1. Introduction

The ocean circulation would look very different without turbulent diapycnal mixing, i.e., mixing across density surfaces, in the ocean interior. Both the horizontal and vertical distribution of diapycnal mixing have been shown to impact various aspects of the large-scale ocean circulation in numerous studies, ranging from idealized simplified models [*Samelson*, 1998; *Munday et al.*, 2011; *Nikurashin and Vallis*, 2012] to comprehensive climate models [*Saenko and Merryfield*, 2005; *Jayne*, 2009; *Canuto et al.*, 2010; *Melet et al.*, 2013a, 2014]. However, turbulent mixing in the ocean interior is poorly represented in present ocean and climate models, and uncertainties in current parameterizations of mixing propagate through the coupled climate system [*Flato et al.*, 2013].

This work is part of an ongoing effort to improve parameterizations of tidal mixing in global climate models. As much as 1 TW of tidal energy could be available for dissipation in the deep ocean [*Munk and Wunsch*, 1998; *Egbert and Ray*, 2000; *Wunsch*, 2000; *Wunsch and Ferrari*, 2004]. The deep-ocean mixing is primarily sustained by breaking internal waves, generated by the interaction of the barotropic tide with the rough seafloor topography. These waves, called *internal tides* (see *Garrett and Kunze* [2007] for a review), extract energy from the barotropic tide, transport it as they radiate away from the seafloor, and dissipate this energy where and when they become unstable and break [*Staquet and Sommeria*, 2002]. The energy loss accompanying wave breaking partly sustains the diapycnal mixing that is ultimately relevant to the ocean global circulation. Consistently, high levels of diapycnal mixing have been observed above rough bathymetry in the deep ocean [*Polzin et al.*, 1997; *Ledwell et al.*, 2000; *Kunze et al.*, 2006; *Whalen et al.*, 2012], but its full three-dimensional (3-D) distribution is still unknown.

In recent climate models, the dissipation of internal tides is often parameterized using the semiempirical scheme formulated by *St. Laurent et al.* [2002]. In this parameterization, the energy flux into internal tides E_0 is consistent with linear wave theory. It is calculated using available bathymetric data set, based on

altimetric observations and sparse acoustic soundings. It therefore only account for waves generated at large-scale satellite-resolved bathymetry. The local dissipation ϵ is then prescribed empirically by considering that a fraction of the energy flux dissipates near the generation site and by specifying a vertical profile of dissipation:

$$\epsilon(x,y,z) \equiv q\, E_0(x,y)\, F(z), \tag{1}$$

where (x, y) denotes the horizontal longitude-latitude coordinates, z height above bottom, and $E_0(x,y)$ the bottom ($z=0$) upward energy flux converted from the barotropic tide into the waves. q is the fraction of energy dissipated locally near the wave generation site, following the vertical distribution F with $\int_0^H F(z)\,dz=1$ ($H(x,y)$ being the local ocean depth). F is typically assumed to be exponentially decaying with a fixed, uniform decay scale. To match observations in the Brazil basin and Hawaiian ridge, a vertical decay scale in the range 300−500 m is usually chosen [*St. Laurent and Nash*, 2004]. The fraction of local dissipation q is set to a constant value of 30% to match observations in the Brazil Basin. While both the fraction and vertical decay scale are held constant in the parameterization, they most likely vary spatially and temporally in the ocean [*St. Laurent and Nash*, 2004; *Waterhouse et al*., 2014].

Sparse observations highlight the spatial heterogeneity of the fraction of tidal energy that is dissipated locally. Large abrupt ridges, such as the Hawaiian ridge, generate energetic internal tides that mostly radiate away, up to thousands of kilometers from their generation site across ocean basins [*St. Laurent and Nash*, 2004; *Zhao et al*., 2012]. A small fraction of local dissipation has been observed over the Mendocino Escarpment (as small as $q=1\%$) [*Althaus et al*., 2003] and over the steep Hawaiian ridge ($q=20\%$) [*Klymak et al*., 2006; *Carter et al*., 2008]. A fraction of local dissipation of $q=10-30\%$ has been inferred from observations in the Drake Passage [*Sheen et al*., 2013], the Kerguelen Plateau [*Waterman et al*., 2013], and the East Pacific rise [*Thurnherr and St. Laurent*, 2011] (also see *Waterhouse et al*. [2014] for a compilation of vertical mixing observations). A larger fraction of local dissipation, $q=40\%$, has been inferred from observations in the East China Sea [*Niwa and Hibiya*, 2004] and at the Luzon Strait [*Alford et al*., 2011]. Rougher small-scale bathymetries (scales of $O(1-10$ km)) generate smaller-scale waves that are more prone to instabilities and local dissipation. A large fraction of local dissipation has consistently been suggested over the rough Brazil Basin, although the value of that fraction differs in the literature as different areas of the Brazil Basin are considered and the definition of local dissipation differs between the studies. Considering a small subset of the Brazil Basin, *Zilberman et al*. [2009] suggested $q=50\%$, while *Polzin* [2004] suggested that internal tides are entirely dissipated ($q=100\%$) within a few tens of kilometers from their generation site in the eastern Brazil Basin.

Therefore, observations strongly suggest that the fraction of local dissipation is impacted by the small-scale topographic roughness. It has recently been noted that the contribution from small-scale, mostly unresolved bathymetry may be particularly important over mid-ocean ridges [*Melet et al*., 2013b]. However current parameterizations of tidal mixing (equation (1)) only account for waves generated at large-scale satellite-resolved bathymetry [e.g., *St. Laurent et al*., 2002; *Simmons et al*., 2004; *Jayne*, 2009]. Here and in the rest of the paper, *small-scale* abyssal hills (or simply abyssal hills) refer to the bathymetry not resolved by satellite altimetry, below $O(10)$ km [*Macdonald et al*., 1996; *Goff et al*., 1996; *Goff and Arbic*, 2010], whereas *large-scale* bathymetry refers to large features resolved in satellite data [*Smith and Sandwell*, 1997]. The fine resolution required to accurately represent the abyssal hill statistics and the large domains required to resolve large-scale bathymetry prevent us from accounting for both, and this paper focuses on small-scale internal tides. It is unknown how abyssal hills contribute to tidal mixing, and this is the question addressed in this study. Of particular interest is whether the spatial distribution of tidal mixing induced by abyssal hills is highly inhomogeneous, since inhomogeneous mixing is known to impact the large-scale ocean circulation. More precisely, the questions that we address are:

1. Can we derive a global map of the fraction of local dissipation of internal tides generated at abyssal hills?
2. What is the associated vertical profile of dissipation? How does it compare to the exponential and power law decays used in parameterizations of dissipation from large-scale topography (equation (1))?

Although direct observations of abyssal hills are not available on a global scale, it is possible to predict the statistical properties of abyssal hill roughness world-wide via the ridge orientation, ridge spreading rate, and sediment thickness [*Goff and Arbic*, 2010]. *Globally* abyssal hills contribute about 10% of the total tidal

energy, but *locally* the energy carried by the small-scale waves can be as large as the energy from large-scale waves [*Melet et al*., 2013b]. This is typically the case at mid-ocean ridges, where abyssal hill roughness is large and where strong bottom mixing levels have been observed [*Polzin et al*., 1997]. In those regions, we expect tidal mixing to be dominated by small-scale abyssal hills, and therefore our results to be close to measured dissipation rates. However, in other parts of the ocean, where abyssal hills are weak or absent, we expect tidal mixing to be dominated by large-scale bathymetry, and therefore our results to largely underestimate the actual dissipation rates. Qualitatively, we believe that the inhomogeneity of the 3-D tidal dissipation and mixing that this work suggests is robust. The addition of the small-scale induced mixing computed here to the large-scale one in current tidal mixing parameterizations (equations (12) and (13)) is discussed in section 5.

Small-scale waves are subject to nonlinear wave-wave interactions, or to fast instabilities such as convective and shear instabilities [*St. Laurent and Garrett*, 2002; *Polzin*, 2004; *Muller and Bühler*, 2009, hereafter MB09; *Polzin*, 2009, hereafter P09; *Nikurashin and Legg*, 2011, hereafter NL11]. The present study aims at estimating the dissipation of internal tides due to convective instabilities (shear instabilities are also briefly mentioned in section 2.2 and supporting information B). These two instabilities have the advantage of being more easily parameterizable (see MB09 and next paragraph), but this implies that the dissipation obtained underestimates the actual one, since we neglect wave-wave nonlinear interactions which are also believed to play an important role in tidal dissipation. Nonetheless, we believe that studying the dissipation of internal tides due to convective instabilities provides one piece of the puzzle with valuable insight into the spatial inhomogeneity of the mixing due to internal tides, and how it may be influenced by geological features such as mid-ocean ridges. Our focus is on predicting the amount and distribution of wave energy radiated at abyssal hills which is dissipated locally near the wave generation site. The remaining fraction of wave energy is assumed to radiate away and its fate is beyond the scope of this study.

Observations of tidal mixing in the abyssal ocean require fine-scale measurements at depth, and are therefore difficult and expensive to obtain. Numerical simulations of internal tides are also challenging, since high resolutions are required to resolve wave breaking and the concomitant turbulence and mixing. These can therefore only be done regionally and in idealized settings. To overcome these limitations, we use theory and a semianalytical tool called *wave saturation* to quantify the direct breaking of internal tides through convective instabilities. This tool, originally introduced in MB09, is computationally efficient and simple enough to be used globally to derive a 3-D map of the dissipation of internal tide energy. The wave saturation is based on the linear wave solution, and on a heuristic model for wave breaking. We extend the work of MB09 to allow for nonconstant stratification. An empirical correction for supercritical bathymetric slopes is also applied. Of particular interest is the relationship between stratification variations, wave amplitudes, and the enhanced energy dissipation in the thermocline observed by *Polzin et al*. [1997].

The paper is organized as follows. Section 2 describes the wave saturation method used to estimate tidal dissipation. Section 3 presents results of a regional study near the mid-Atlantic ridge, where the dissipation profile obtained from the wave saturation is compared to observations. In section 4, the global three-dimensional map of tidal dissipation over abyssal hills is derived. Implications for parameterizations of tidal mixing in climate models are then discussed in section 5. Conclusions and limitations of this study are presented in section 6. Readers interested in the global results can proceed directly to sections 4–6.

2. The Wave Saturation Method

In this section, we briefly describe the wave saturation method. The idea behind this method, based on the saturation of the linear wave amplitudes, is to use linear theory to predict its own breakdown. In this section, we describe the method in detail. In a first step, the internal wavefield above a given bathymetry is computed according to linear theory. Where large unstable wave amplitudes are found, they are saturated to a lower stable value, thereby modeling wave breaking. The stable wavefield is then propagated upward by a small increment, checked for instability, saturated if necessary, and so forth. Once the waves reach the ocean surface, the vertical energy flux lost through the saturation process is computed, yielding an estimate

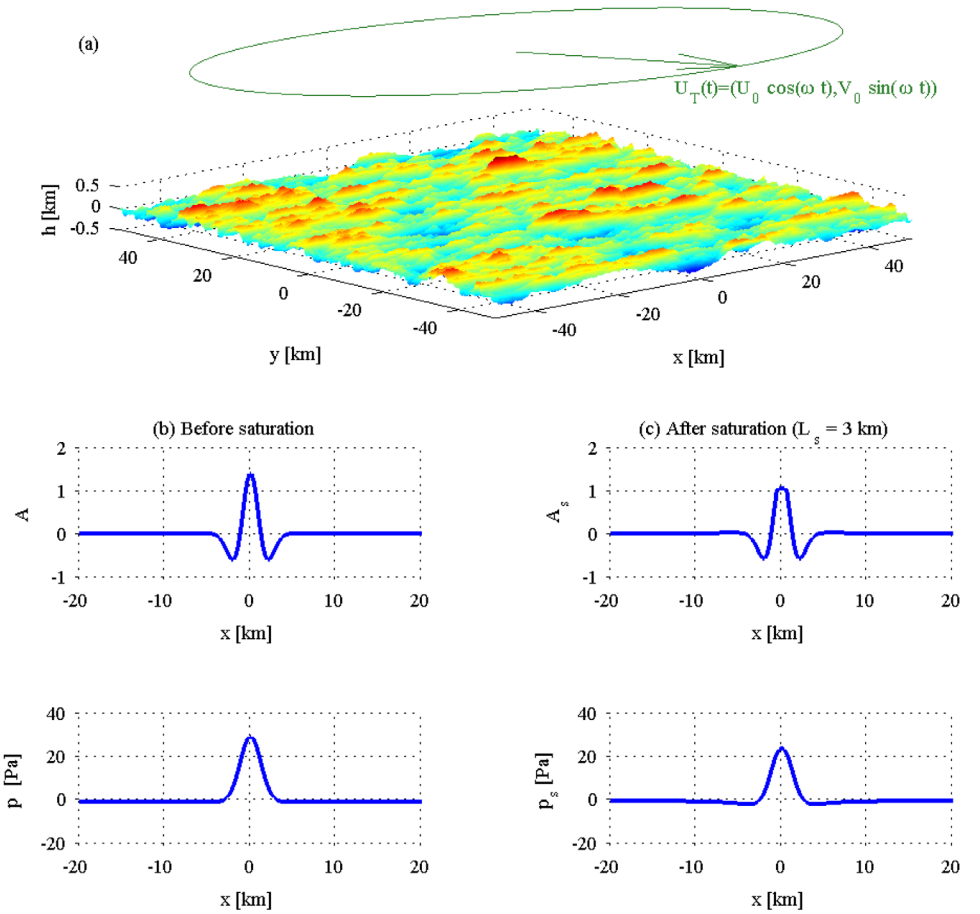

Figure 1. (a) Schematic illustration of the setting; the barotropic tide oscillates above the bathymetry with velocity $\mathbf{U}_T(t)=(U_0\cos\omega t, V_0\sin\omega t)$, where ω denotes the tidal frequency, about twice a day for the largest lunar semidiurnal tide. (b and c) Illustration of the wave saturation in the case of an idealized isolated topography (idealized example from MB09, see their Figure 1). Figure 1b shows the unstable amplitude A and corresponding pressure p; Figure 1c shows the corresponding fields A_s and p_s once saturation has been applied.

of energy dissipation from wave instability and breaking in the whole water column. Originally introduced by MB09 for constant stratification, we extend this method to allow for vertical variations in the stratification.

2.1. Wave Generation

The setting is illustrated in Figure 1a. The barotropic tide oscillates above the bathymetry with velocity $\mathbf{U}_T(t)=(U_0\cos\omega t, V_0\sin\omega t)$, where ω denotes the tidal frequency, about twice a day for the largest lunar semidiurnal tide. Since we are interested in the local, fast instabilities of small-scale internal tides, we suppose that the ocean depth is infinite, which is appropriate for small-scale waves believed to be dissipated quickly, before they reach the ocean surface [*St. Laurent and Garrett*, 2002]. The bathymetry is assumed to be subcritical, i.e., its slope is everywhere smaller than the slope of the wave characteristics [*Bell*, 1975a,b; *Garrett and Kunze*, 2007]. Even with these simplifications, the problem is known to be difficult, and it is common to make the small excursion approximation, i.e., to assume that the tidal excursion distance $||\mathbf{U}_T||/\omega$ is small compared to the horizontal extent of the bathymetry [*Llewellyn Smith and Young*, 2002; *Bühler and Muller*, 2007]. Nevertheless, since it is not valid at the small bathymetric scales relevant for the instabilities addressed here (MB09), we shall *not* make this approximation. Importantly, we however only consider the wave response at the fundamental tidal frequency ω, which dominates the wavefield [*Melet et al.*, 2013b]. The linear wave solution under those conditions can be derived in Fourier space, and is recalled in supporting information A for constant and for slowly varying stratification.

2.2. Wave Breaking and Saturation

Prior to saturating the linear solution, we need a variable capable of signaling unstable wavefields. The convective instability is captured by the nondimensional wave amplitude A, also referred to as "wave steepness" in the literature [*Staquet and Sommeria*, 2002]. A is related to the density gradient $\partial\rho/\partial z$:

$$-\frac{g}{\rho_0}\frac{\partial\rho}{\partial z} \equiv N^2\left\{1-\mathrm{Re}\left[A(x,y,z)\,\mathrm{e}^{-i\omega t}\right]\right\}, \tag{2}$$

where ρ_0 denotes a reference density and N the mean stratification. If $|A| > 1$, overturning of the isopycnals ($\partial\rho/\partial z > 0$) occurs at some time of the tidal period and the linear waves are unstable. This signals convective instability, but one could introduce a similar amplitude to equation (2), based on the Richardson number, that would signal shear instability. The associated technical difficulties are exposed in supporting information B and we shall focus on convective instability in most of the rest of the paper.

In order to model wave breaking, we saturate the waves, i.e., we enforce $|A| \leq 1$, as illustrated in Figure 1 which shows an unstable wave amplitude and corresponding pressure (Figure 1b), and the saturated fields (Figure 1c). If the two-dimensional (2-D) bottom amplitude $A(x,y,z=0)$ is unstable, saturation is applied and yields the stable amplitude $A_s(x,y,z=0)$. At each altitude z, $A_s(x,y,z)$ is then propagated upward by a small vertical increment dz to yield $A(x,y,z+dz)$, which is in turn checked for instability and saturated if necessary before being propagated further up. Thus, only stable waves are allowed to propagate in the ocean interior, and breaking and energy dissipation are resolved three dimensionally.

The saturation method requires two free parameters. The first one is the amplitude threshold at which saturation occurs a_s. Overturning occurs when $|A| > 1$ suggesting an amplitude threshold $a_s = 1$, which is what shall be used in the following. However, overturning does not always imply wave breaking, suggesting $a_s \gtrsim 1$. The second parameter is the saturation length L_s. Mathematically, the saturation method is a nonlocal procedure (a convolution, in physical space) performed around the instability over a domain of size L_s. Physically, L_s may be thought of as the horizontal extent over which the wavefield is impacted when a wave breaks. MB09 pick $L_s = O(3-5$ km) based on a maximization of the energy loss at the bottom. This criterion is not practically usable in our global computation due to the high computational cost of trying several values of L_s in order to find the optimal one (maximizing the dissipation) at each location. Instead, we use a criterion based on the spatial scale of the maximum wave amplitude. L_s may indeed be intuitively related to the scale of the most unstable wave, whose breaking is expected to have an imprint of a few times its horizontal wavelength L_A. A more detailed study suggests that the maximum bottom energy loss occurs when $L_s \sim 3\times L_A$. Hence, we set $L_s = 3\times L_A$ in our model. More details about the whole generation and saturation algorithm as well as the saturation method (how to implement $|A| \leq 1$) are given in supporting information A. Our results are found to be robust to reasonable changes in the two free parameters a_s and L_s (see supporting information C).

2.3. Energy Dissipation

We are interested in the vertical profile of the energy dissipation rate ϵ, averaged over time (over one tidal period) and over a given horizontal domain (see section 3.1 for information about the spatial domain):

$$\epsilon(z) \equiv -\frac{\partial E_s}{\partial z}, \tag{3}$$

where E_s denotes the saturated vertical energy flux $\rho_0 < p_s w_s >$ and $<.>$ the time and horizontal average. Nonzero dissipation due to wave breaking is achieved in our model by wave saturation ($\partial E_s/\partial z \leq 0$). Note that without wave breaking, $\epsilon(z) = 0$, since the vertical energy flux of linear waves is nondivergent.

2.4. Correction for Supercritical Slopes

It has been suggested that the energy flux plateaus as the nondimensional parameter $\gamma = ||\nabla h||/s$, which determines the criticality of the bathymetry (ratio of the slope of the bathymetry to the slope of the wave characteristics s), reaches unity [*Khatiwala*, 2003; *Nycander*, 2006; *Balmforth and Peacock*, 2009].

Based on this observation, a rescaling of the energy flux in $1/\gamma^2$ at supercritical bathymetry (i.e., when $\gamma > 1$) has been proposed [*Melet et al.*, 2013b; *Falahat et al.*, 2014]. We apply this correction locally for supercritical slopes in our estimates by reducing the bathymetry spectrum (given by equation (4) for the

mid-Atlantic ridge region, and more generally by equation (1) of *Goff and Arbic* [2010] for global abyssal hills) by a factor $1/\gamma^2(\kappa)$ if $\gamma(\kappa) > 1$, with $\gamma(\kappa)=(\kappa/2\pi)h/s$ and $\kappa=\sqrt{k^2+l^2}$, the local bathymetric wave number. This operation reduces the energy flux into internal tides, and we find that it reduces the dissipation slightly, but does not change the qualitative results of this paper.

3. Regional Study: Application to the Mid-Atlantic Ridge

3.1. Setting: Tidal Forcing, Bathymetry, and Stratification

The goal of this section is to test the wave saturation against the observational results of *Polzin et al*. [1997] in the Brazil Basin near the mid-Atlantic ridge. The barotropic M_2 tidal forcing is $(U_0, V_0)=(2.1\ \text{cm s}^{-1}, 2.5\ \text{cm s}^{-1})$, with tidal frequency $\omega=1.45\times10^{-4}\ \text{s}^{-1}$, and at this latitude (about 21.5°S), the Coriolis frequency is $f=-5.3\times10^{-5}\ \text{s}^{-1}$.

As mentioned in section 1, we focus on internal tides generated by small-scale bathymetry (abyssal hills), with horizontal scale below 10 km or so [e.g., *Macdonald et al*., 1996]. Global maps of the seafloor from satellite altimetry only contain large-scale bathymetric features, with a resolution above 10 km [*Smith and Sandwell*, 1997]. Small-scale bathymetry is only known deterministically where acoustic soundings were performed, representing only 10% of the global ocean seafloor, mostly located in coastal zones [*Charette and Smith*, 2010]. Consequently, we follow MB09 and NL11 and take a statistical approach (described below in equation (4)) to represent the bathymetry. In this region above the mid-Atlantic ridge, abyssal hill roughness is large. We therefore expect tidal dissipation to be dominated by waves from small-scale bathymetry and our results should be close to measured dissipation rates over this region. This is consistent with the numerical simulations of NL11 who also only include internal tides generated by abyssal hills, and recover the observed dissipation rates.

Goff and Arbic [2010] propose the following 2-D spectrum for small-scale bathymetry based on geological constraints:

$$C(k,l) \equiv \frac{4\pi\nu h^2}{l_0 k_0}\left(\frac{k^2}{k_0^2}+\frac{l^2}{l_0^2}+1\right)^{-(\nu+1)}. \tag{4}$$

For the region of the mid-Atlantic ridge studied here, the bathymetric roll-off wave numbers are $k_0=2.2\times10^{-4}\ \text{m}^{-1}$ and $l_0=1.0\times10^{-3}\ \text{m}^{-1}$, $\nu=0.9$ determines the roll-off slope at high wave numbers, and the root-mean-square (rms) height of the bathymetry is $h = 110$ m (P09). For a given spectrum, the simplest bathymetry that can be statistically generated in physical space is a random Gaussian field. We first draw 10 independent, random, square bathymetry realizations (or samples) of typical horizontal size $O(50\ \text{km})$ and resolution of $O(100\ \text{m})$. Using vertical steps of $O(50\ \text{m})$, we then compute the whole energy flux profiles and the corresponding dissipation $\epsilon(z)$ for each bathymetry and average the results among the samples to get a mean profile of energy dissipation. As long as the spatial domains are large enough, we find little spread of the profile of energy dissipation over the 10 independent realizations (see the gray shading in Figure 3).

Figure 1a illustrates one realization of the bathymetry. Note that the spectrum is not isotropic, reflecting the anisotropy of abyssal hills (they tend to be aligned alongside the ridge where they are formed). In this region, the bathymetry is smoother in the x direction and rougher in the y direction.

For the stratification, an analytical fit of $N(z)$ to the observed profile in this region is used, similar to NL11 (see their Figure 4).

3.2. Instability of the Linear Solution at the Seafloor

We first look at the linear solution at $z = 0$. For those bottom values, we focus on the y direction since it is the direction where bathymetry is the roughest (Figure 1a). Looking at cross sections in two dimensions (x, z) or (y, z)—where the one-dimensional $c(k)$ or $c(l)$ spectrum is obtained from the 2-D spectrum by integration (MB09)—reveals that the waves in the x direction are stable, while the waves in the y direction are unstable. The amplitude of the whole 3-D wavefield is very close to the 2-D amplitude in the y direction. Physically, this means that the waves are nearly 2-D, and that overturning occurs in the y direction. Therefore, in this section, we neglect any x dependence and investigate the bottom fields $A_0(x,y) \approx A_0(y)$. This allows us to highlight

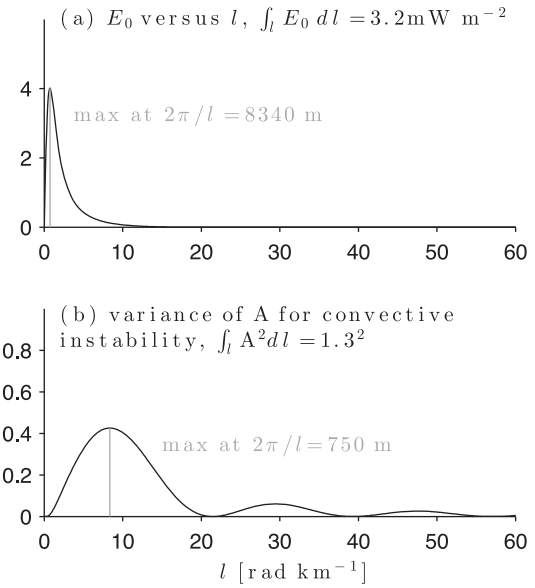

Figure 2. Regional study over the mid-Atlantic ridge: linear waves at the seafloor. (a) Energy flux and (b) squared amplitude for convective instability at $z = 0$ versus horizontal wave number l (in the y direction). Note that internal tides are stable wave number by wave number ($A^2(l) < 1$), but their superposition is not ($\int_l A^2\,dl = 1.3^2 > 1$).

the scales in y which dominate the wave energy and the wave breaking. We will come back to the full 3-D problem once wave saturation is applied (section 3.3) and instabilities in the y direction affect the whole 3-D wavefield.

Figure 2 shows the energy flux as a function of wave number l in the y direction, and the rms amplitude for convective instability ($A_0(y)$ in equation (2), see also MB09 equations (8) and (9)). We see that the wave energy dominantly comes from bathymetries with scales $O(10$ km), while the scales responsible for instabilities are smaller, around $L_A = O(1$ km). The fact that the wave amplitude is large at small bathymetric scales is consistent with the consensus that small-scale waves are more easily subject to fast, local dissipation. Mathematically, it can be understood from the expression for the variance of amplitude as a function of the one-dimensional bathymetric spectrum, $c(l) = \int C(k,l)dk/2\pi$ (MB09): $|A|^2 \propto \int [l\,J_1(V_0 l/\omega)]^2 c(l)dl$, where $J_1(x)$ is the Bessel function of the first kind of order 1. The factor $l\,J_1(V_0 l/\omega)$ amplifies small scales.

It has been pointed out in the literature [*St. Laurent and Garrett*, 2002; NL11] that wave number by wave number, the amplitudes for shear or convective stability are smaller than unity and waves could therefore be considered as stable. Our results also show that wave number by wave number, internal tides are stable with regard to convective (and shear) instabilities. However, once we allow for constructive interference between scales (by integrating over all wave numbers), the amplitude has a rms larger than unity ($\int_l A^2\,dl = 1.3^2$ as shown in Figure 2), i.e., the wavefield at $z = 0$ is unstable.

3.3. Saturation and Vertical Profile of Energy Dissipation

We now apply wave saturation. The scale of maximum amplitude being $L_A \sim 1$ km, we set the saturation length to $L_s = 3L_A = 3$ km. At $z = 0$, the waves from linear theory are unstable, and yield a bottom dissipation $E(0) - E_s(0) = 3.2 - 2.1 = 1.1$ mW m^{-2}, corresponding to 34% loss.

The energy flux before saturation $E(0)$ cannot easily be compared to observations or simulations, since the unstable linear wavefield would almost instantaneously break and adjust to a stable configuration. The energy flux after saturation $E_s(0) = 2.1$ mW m^{-2} is broadly consistent with the bottom energy flux of 1.8 mW m^{-2} found in numerical simulations for the same bathymetry and forcing (NL11), though slightly higher. This may be due to the absence of nonlinear effects in the boundary layer, such as flow separation from seafloor or hydraulic jumps.

The vertical profile of energy dissipation $\epsilon(z)$ predicted by the wave saturation method with constant stratification ($N = N_{bottom}$) is shown in Figure 3. Also shown for comparison are the in situ observations of *Polzin et al.* [1997]. Wave saturation captures the general behavior of the dissipation profile in the deeper part of the water column, up to 2 km above the seafloor, though it underestimates its magnitude in the first kilometer (compare the blue line and purple circles in Figure 3b). This may be because wave saturation only accounts for wave breaking through convective instability, and neglects wave-wave interactions, which likely contribute to the observed profile as well. We assessed the importance of the shear instability in supporting information B. We found that, for the region studied here, the shear instability is either negligible or yields similar results as the convective instability. Accounting for both instabilities generally does not provide additional insight, since once the wavefield is saturated with respect to one amplitude, it is stable with respect to the other. This motivates us to concentrate on convective instability for the global study in the next section.

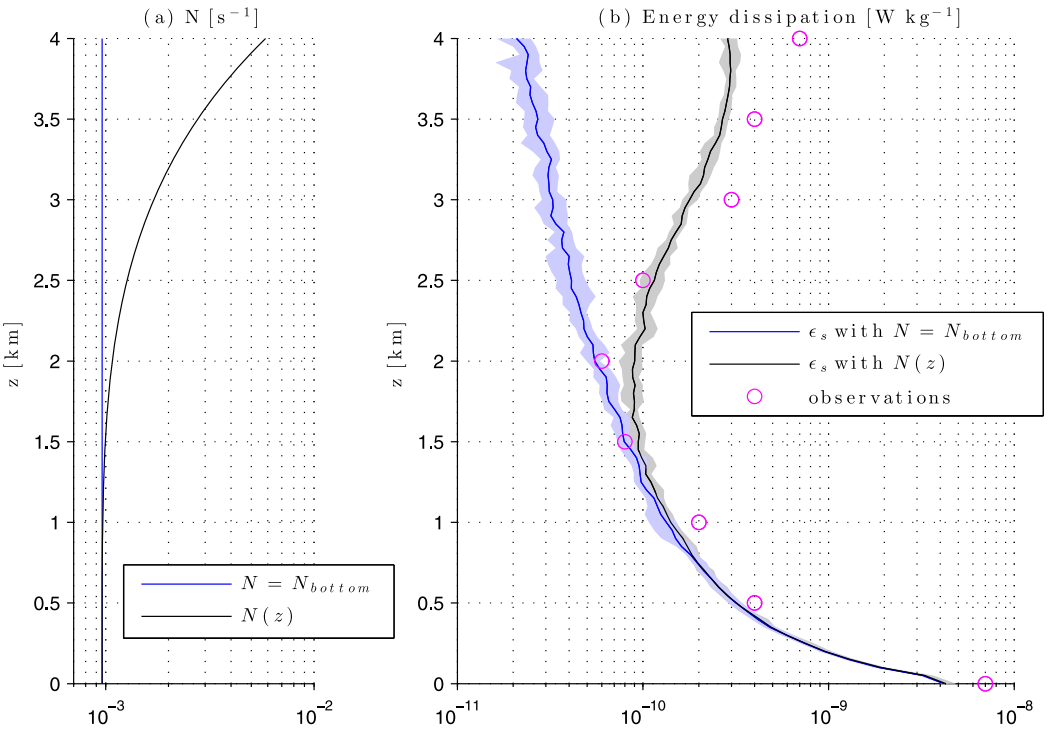

Figure 3. Regional study over the mid-Atlantic ridge: wave saturation. Vertical profiles of (a) stratification and (b) wave energy dissipation through wave saturation, with constant (blue) and varying (black) stratification $N(z)$. The vertical profile $N(z)$ is an analytical fit to observations in the region studied in section 3 [*Polzin et al.*, 1997] (similar to the profile used in NL11). Observed dissipation profiles [*Polzin et al.*, 1997; P09] are also shown in Figure 3b for comparison. The gray shading shows the spread (min and max) of estimates from the 10 bathymetric samples.

When variations of the stratification are accounted for (Figure 3), the agreement is improved above 2 km above the seafloor, where stratification variations become important (compare the black line with the purple circles in Figure 3b). In particular, wave saturation captures the increase of energy dissipation associated with the increase in stratification expected from the theory of internal tides. As recalled in supporting information A, the slope of the characteristics along which these waves propagate decreases when N increases as $s=|\kappa/m| \propto (N^2(z)-\omega^2)^{-1/2} \approx N(z)^{-1}$, where m and κ are the vertical and horizontal wave numbers, respectively (the last approximation follows from the fact that in typical oceanic conditions $N/\omega \gg 1$). Above a given bathymetry, the vertical lengthscale of the waves thus decreases as $N^{-1}(z)$, and the asymptotic WKB theory predicts that their amplitude increases as $A \propto \sqrt{m} \propto \sqrt{N(z)}$. In other words, an increasing stratification yields smaller-scale waves of larger amplitudes that are more prone to overturn and break. Our results suggest that enhanced energy dissipation in the thermocline can be sustained by the dissipation of internal tides radiated at the seafloor, in addition to internal waves generated at the surface of the ocean. Our analytical dissipation profile is close to but does not exactly match observations, which is likely due to the simplifying assumptions of our approach. Yet, given the simplicity of our model, we believe that the agreement is encouraging. We apply this methodology in section 4 over the global ocean.

4. Global Map of Tidal Dissipation

Unlike observations and numerical simulations, the wave saturation method has the advantage of being simple enough (it only involves the fast Fourier transform and its inverse) that it can be applied globally. In this section, we use it to derive a first 3-D world map of abyssal-hill generated internal-tide dissipation and of the induced diapycnal mixing.

4.1. Setting: Tidal Forcing, Bathymetry, and Stratification

We use M_2 tidal data from the TPXO 7.2 model of *Egbert and Erofeeva* [2002] assimilating TOPEX/Poseidon satellite radar altimetry data. The semidiurnal lunar tidal flow with frequency ω obeys an ellipse of

parametric equation $[U_0\cos(\omega t), V_0\sin(\omega t), 0]$ and major axis orientation angle θ with respect to the North. Global $1/4^\circ \times 1/4^\circ$ maps of U_0, V_0, and θ were obtained using the Tide Model Driver (TMD) toolbox of *Egbert and Erofeeva* [2002]. Only the waves generated at the fundamental frequency ω are retained, as higher harmonics only account for a minor fraction of the energy conversion [*Melet et al*., 2013b].

As in the mid-Atlantic ridge study, we only include the small-scale bathymetry, i.e., abyssal hills with horizontal scales below $O(10$ km). We use the spectrum proposed by *Goff and Arbic* [2010] (their equation (1)), thereafter referred to as *GA spectrum*, which predicts statistical features of abyssal hills, such as height covariance or anisotropic roughness from geological observations. The four parameters of the GA spectrum, the rms height of the hills, the local spreading axis angle with respect to longitude and latitude, and their roughness normal and parallel to it, were provided by A. Goff and B. Arbic and vary in space at a $1/4^\circ \times 1/4^\circ$ resolution. With typical values of domain size $L = O(50$ km), horizontal resolution $dx = dy = O(100$ m) and vertical wave propagation/saturation increments $dz = 50$ m, a global computation required about a week on a 16-core workstation. The parameters of the saturation model have been chosen as in the regional study. More details about the computation and its sensitivity to parameters are given in supporting information C.

The global buoyancy frequency $N(x, y, z)$ is obtained by processing the World Ocean Circulation Experiment (WOCE) 2004 data with the Gibbs Sea Water (GSW) toolbox [*McDougall and Barker*, 2011]. Interpolation was performed from the original $1/2^\circ \times 1/2^\circ$ to the $1/4^\circ \times 1/4^\circ$ resolution of the GA spectrum, which is the resolution used in our computations.

4.2. Horizontal Distribution of Local Dissipation

The horizontal distribution of the bottom energy flux E_0 in equation (1) converted by abyssal hills into internal tides is shown in Figure 4a. The bottom energy flux is computed using linear theory as in section 3, with the spectrum in equation (4) replaced by the GA spectrum at each location where the abyssal hill distribution is available (locations not in white in Figure 4, see *Goff and Arbic* [2010] for details). Where E_0 reaches unrealistic large values due to poor tidal data in shallow regions (few locations near Iceland), a bottom capping of $E_0^{\mathrm{cap}} = 10^{-1}$ W m^{-2} is enforced. Regions of high barotropic energy conversion are found to concentrate around mid-ocean ridges, where the hills are tallest and roughest. The conversion integrates to 105 GW globally (standard deviation among the 10 samples is < 0.1 GW), which is consistent with the earlier estimate of *Melet et al*. [2013b].

We now turn to the fraction of local dissipation q in equation (1), defined as the energy lost through saturation when waves propagate from the seafloor to $z = H$:

$$qE_0 = \int_0^H \epsilon \, dz, \tag{5}$$

where H is the ocean surface, unless a reflection level is reached before the surface ($N(z) = \omega$). In the latter case, the waves are reflected back down [*Sutherland*, 2010] (this effect is ignored in our computation) and H is set to the depth of the reflection level. The fraction of local dissipation is computed only at locations with nonnegligible wave energy $E_0 > 10^{-5}$ W m^{-2} (not in gray in Figure 4).

The distribution of q is shown in Figure 4b. Interestingly, its spatial distribution is far from homogeneous. Vast regions exhibit very high values of q, between 60% and 90%. Mostly located in the Southern Hemisphere, these include the mid-Atlantic ridge, the central Indian ridge, and the East Pacific rise, and are surrounded by regions where q decays but still exceeds 30%. Elsewhere in the deep ocean where abyssal hill data are available, the fraction of local dissipation is lower than 10%. Globally, the energy dissipation amounts to 64 GW, that is, 61% of the barotropic conversion by abyssal hills. About 80% of this dissipation occurs at regions where $q > 60\%$. The map of the depth-integrated energy dissipation qE_0 can be found in supporting information E.

This estimate of q only includes waves generated by abyssal hills, i.e., q is the fraction of wave energy radiated at abyssal hills which is dissipated through convective instability of those small-scale waves. We can estimate the fraction of the *total* energy, including both small and large-scale waves, which is dissipated through the instability of small-scale waves

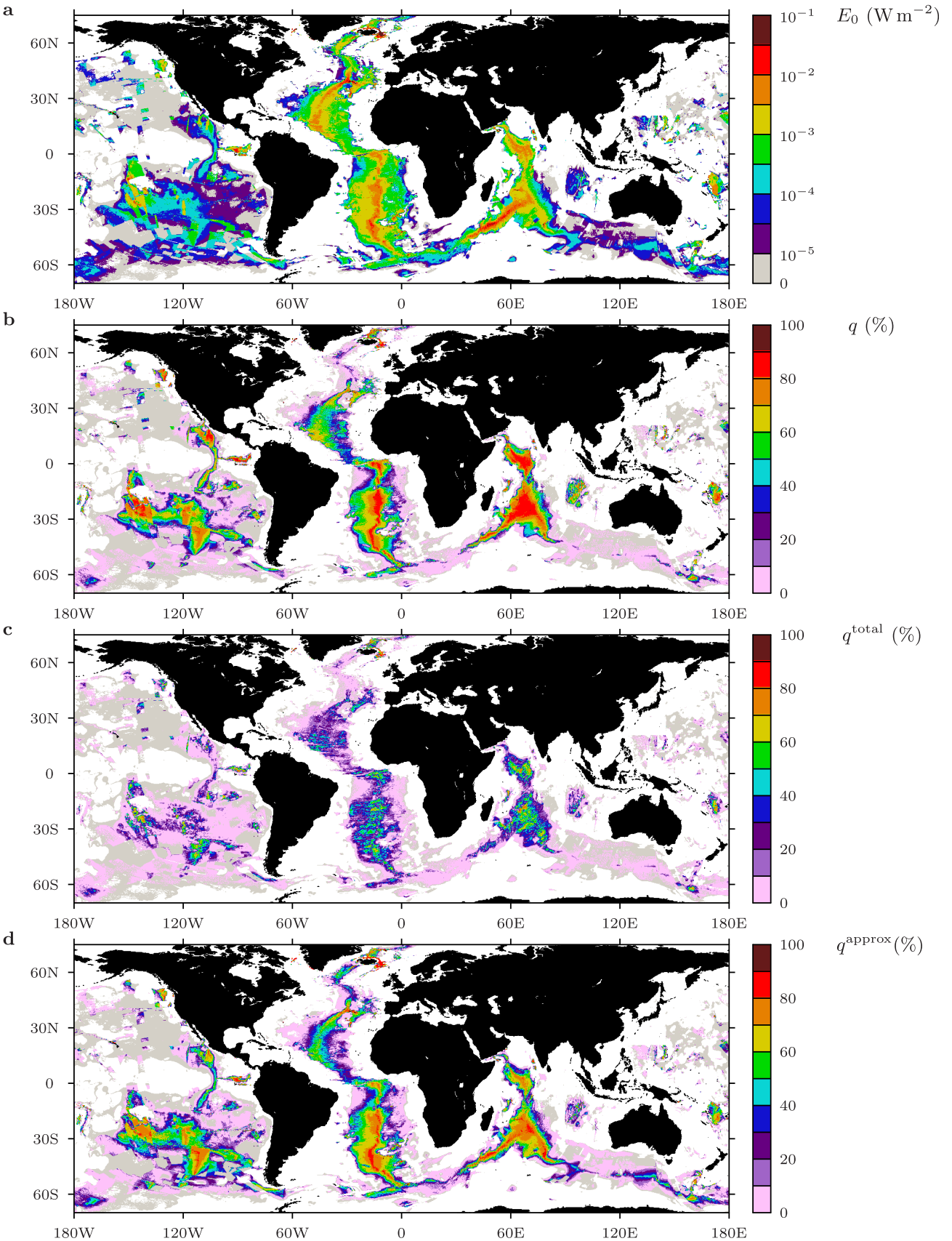

Figure 4. Horizontal distribution of the tidal energy dissipation. (a) Bottom vertical energy flux E_0 converted by abyssal hills into internal tides. (b) Fraction of local dissipation q of E_0. (c) Fraction q^{total} of the total flux $E_0+E_0^{\mathrm{large\,scale}}$ dissipated locally (equation (6)). (d) Approximation q^{approx} of q using the rms bottom amplitude $A^{\mathrm{rms}}(0)$ (equation (8)). Smooth regions with no bathymetry data (no abyssal hill) are shown in white. Regions where $E_0 < 10^{-5}$ W m^{-2} are shown in gray. All data are at $1/4^\circ \times 1/4^\circ$ resolution.

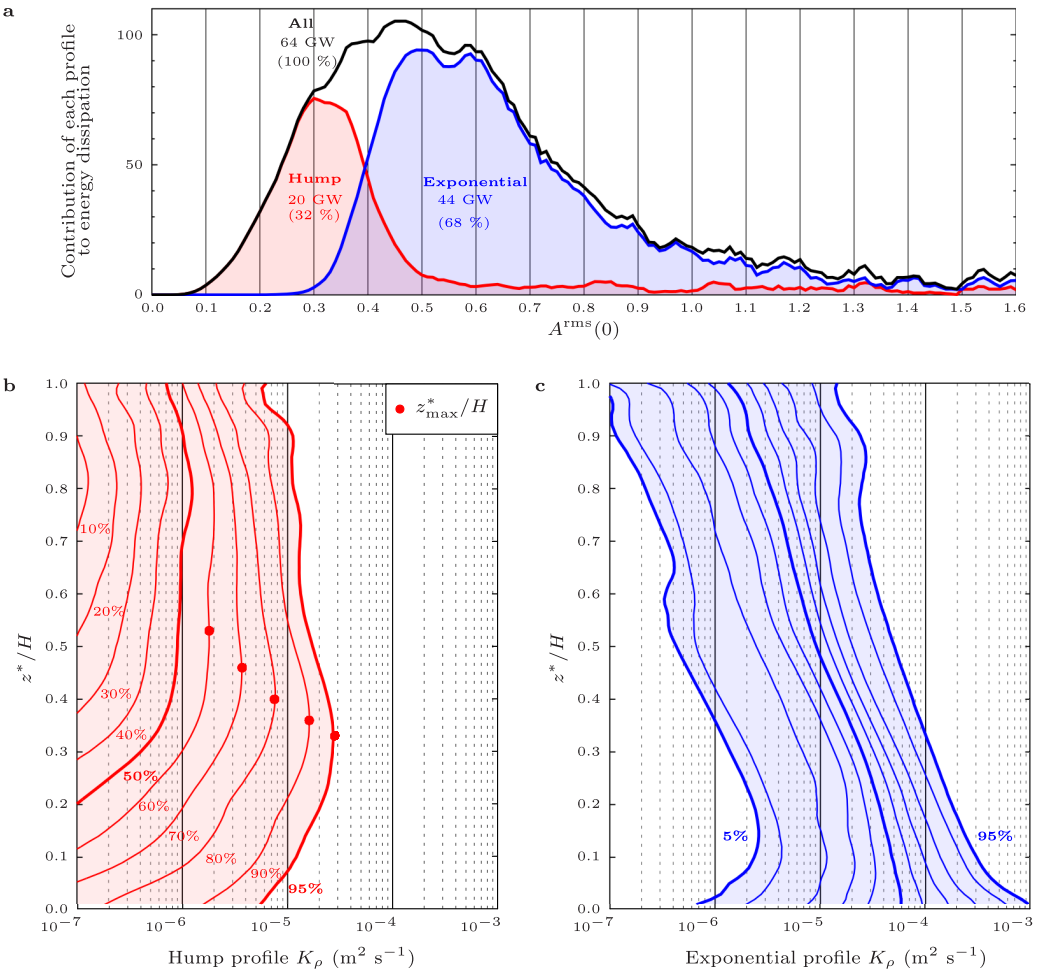

Figure 5. Existence of two vertical profiles of dissipation. (a) Distribution of energy dissipation with respect to $A^{\mathrm{rms}}(0)$ and contribution of each profile. The integral is the total dissipated energy 20+44=64 GW. Exponential and hump profiles may be separated by the value $A^{\mathrm{rms}}(0)=0.4$. (b) Percentiles (with respect to energy dissipated) of all hump profiles of K_ρ (50% curve corresponds to median profile). Note the transition from midlevel maxima (most energetic percentiles) to profiles with no bottom mixing and constant upper-level mixing. (c) Percentiles of vertical profiles of K_ρ for exponential profiles. Note the logarithmic scale for the diapycnal diffusivity in Figures 5b and 5c.

$$q^{\mathrm{total}} \equiv \frac{qE_0}{E_0+E_0^{\mathrm{large\,scale}}}. \tag{6}$$

If the waves generated by large-scale bathymetry did not contribute to the local dissipation and entirely propagated away from their generation site, q^{total} would be the total fraction of local dissipation. Small-scale waves have been observed to dominate the local dissipation in places, for instance, *St. Laurent and Nash* [2004] suggest that the dissipation level scales with the energy available in the high modes (i.e., scales smaller than roughly 10–20 km for modes 5–10, see their Figure 5). In the region over the mid-Atlantic ridge that they study, 75% of the energy is contained in modes higher than 5 (scales smaller than about 20 km). However, in general, we expect q^{total} to be a lower bound for the total fraction of local dissipation (see section 5 for a more in-depth discussion).

The distribution of q^{total} is shown in Figure 4c. The same hotspots emerge, albeit with lower magnitudes (20–60%) and more patchiness, reflecting the patchiness of $E_0^{\mathrm{large\,scale}}$ [*Melet et al*., 2013b]. Since abyssal hills contribute about 10% of the global conversion ($E_0^{\mathrm{large\,scale}} \sim 875$ GW), the global average fraction drops to 6% or 17% restricting the computation to the regions having some small-scale dissipation (not in gray or white in Figure 4).

We find that q is not only sensitive to the bathymetry, but also to the tides and stratification. This dependence may be reasonably well understood from the rms bottom linear wave amplitude [*Bell*, 1975b; MB09]

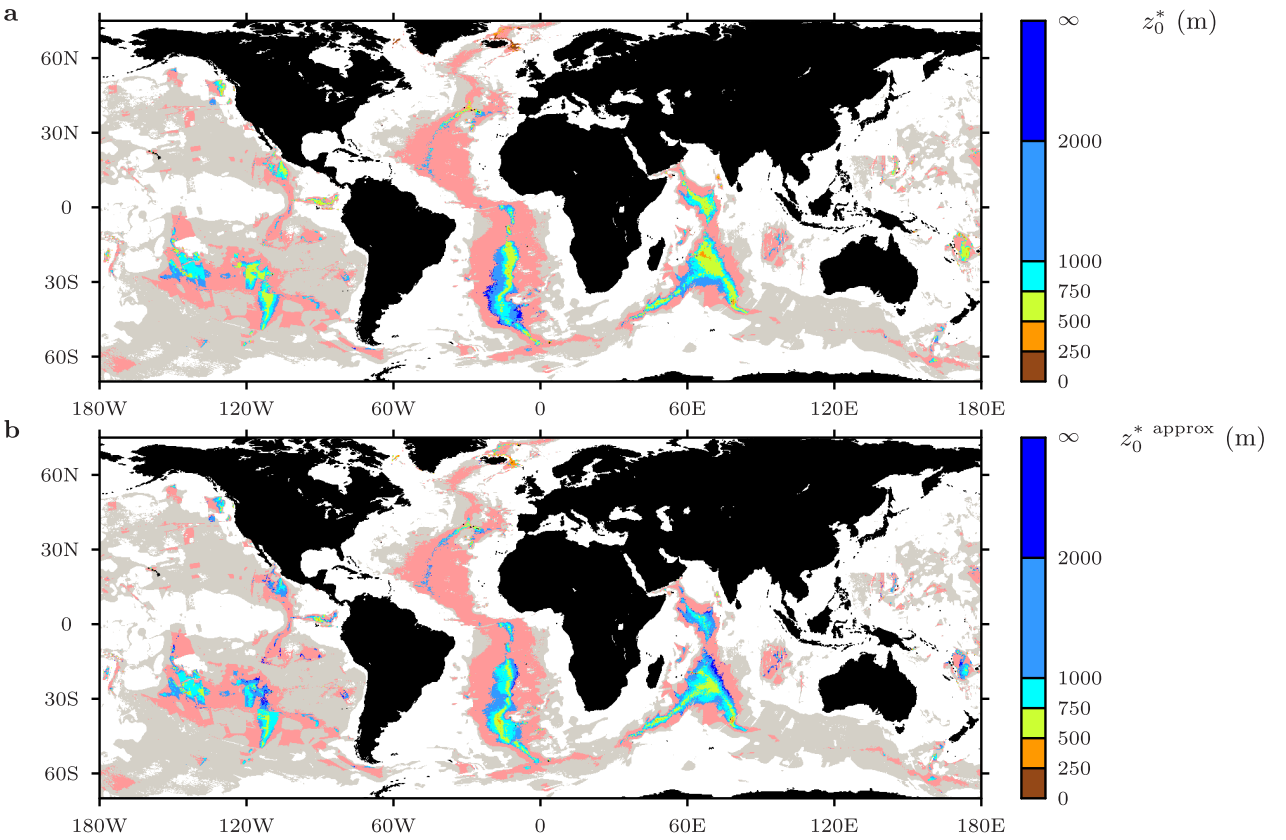

Figure 6. Decay scale of the exponential profiles. (a) *e*-folding value z_0^* determined by the linear regression on exponential profiles of $\log(K_\rho)$ with WKB-scaled z^* coordinate. White stands for no abyssal hills as in Figure 4. Gray now indicates little dissipation $qE_0 < 10^{-5}$ W m^{-2}. Pink indicates regions of hump profiles. (b) $z_0^{*\,\mathrm{approx}}$ predicted by the bottom amplitude $A^{\mathrm{rms}}(0)$ (equation (10)). All data are at $1/4^\circ \times 1/4^\circ$ resolution.

$$A^{\mathrm{rms}}(z=0)=\sqrt{\frac{N(z=0)^2-\omega^2}{(\omega^2-f^2)\pi^2}\int_{\mathbb{R}}\int_{\mathbb{R}} C(k,l)(k^2+l^2)J_1^2\left(\frac{\sqrt{U_0^2K^2+V_0^2L^2}}{\omega}\right)dk\,dl}, \tag{7}$$

where $(K,L)=(k\cos\alpha-l\sin\alpha, k\sin\alpha+l\cos\alpha)$ is the wave number vector in the frame of the tidal ellipse (see MB09 and supporting information A). By fitting the relationship between q and $A^{\mathrm{rms}}(0)$ of our results (see supporting information D), we derive the following simple empirical formula for q:

$$q^{\mathrm{approx}}=\begin{cases} 87\{1-\exp[-4(A^{\mathrm{rms}}(0)-0.1)]\} & \text{if } A^{\mathrm{rms}}(0)>0.1 \\ 0 & \text{otherwise.} \end{cases} \tag{8}$$

Figure 4d shows that, despite solely relying on a *linear* measure of wave instability *at the bottom*, q^{approx} captures the main features of the distribution of q. This expression also reproduces the total dissipation (65 GW instead of 64 GW; see supporting information D for more details).

4.3. Vertical Distribution of Dissipation and Mixing

We now turn to the vertical structure of tidal dissipation $F(z)$ in equation (1). We consider our profiles of $F(z)$ to see if they have a universal shape in the vertical, such as the exponential proposed by *St. Laurent et al*. [2002] or a power law such as P09. To seek universal profiles, the influence of the varying buoyancy frequency $N(z)$ is reduced by stretching the vertical coordinate z to z^* using the WKB theory [*Gill*, 1982]

$$z^* = \frac{\int_0^z \sqrt{N^2(z') - \omega^2}\, dz'}{\frac{1}{H}\int_0^H \sqrt{N^2(z') - \omega^2}\, dz'}. \quad (9)$$

As this coordinate stretching is insufficient, we further rescale F by a power of N. The scaling F/N^2 proves to be the best to collapse profiles (see supporting information D), which is consistent with earlier studies [see *Polzin et al*., 1995, and references therein]. Thus, to ease comparison with the literature, we present results for the diapycnal diffusivity $K_\rho = \Gamma\epsilon/N^2$ [*Osborn and Cox*, 1972], with a mixing efficiency $\Gamma = 0.2$. Since both exponential [*St. Laurent et al*., 2002] and power law (P09) decaying profiles have been suggested for K_ρ, we carry a linear regression of $\log(K_\rho)$ in the z^* and $\log(z^*)$ spaces. We restrict our analysis of vertical profiles to points with some dissipation $qE_0 > 10^{-5}$ W m^{-2} (not in gray in Figure 6).

We find that the fit is better in the exponential case. However, not all the points obey this exponential decay. We consider that a profile is exponentially decaying if the regression to $K_\rho(z^*) = K_\rho(0)\, e^{-z^*/z_0^*}$ leads to $z_0^* > 0$ and to a coefficient of determination $R^2 > 0.6$ (see supporting information D for details and examples of profiles).

According to this criterion, exponentially decaying profiles are found in 25% of the area covered by dissipation and are responsible for 68% of the dissipated energy. The remaining profiles, covering the remaining 75% area and dissipating 32% of the energy, have in common to be nonmonotonic and many possess a midlevel "hump," hence the subsequent name *hump profile*.

The bottom-enhanced diffusivity of exponential profiles is due to high bottom wave amplitudes, which are more likely to be unstable close to their generation site. Hump profiles by contrast exhibit stronger diffusivity higher up in the water column due to increased stratification. We therefore expect exponential profiles to dominate where the bottom amplitudes are large and vice versa. This is confirmed by Figure 5a, showing the distribution of the dissipated energy with respect to the rms amplitude of the linear waves $A^{\mathrm{rms}}(0)$. Although Figure 5a shows some overlap, the two profiles may be reasonably well diagnosed a priori according to the following criterion: if $A^{\mathrm{rms}}(0) > 0.4$, the diffusivity decays exponentially, otherwise it follows a hump profile.

4.3.1. Exponential Profiles

The analysis of percentiles of the whole distribution of exponential profiles is shown in Figure 5c. The most energetic profiles follow almost perfect exponential decay, and half of the energy (~22 GW) is indeed found to be dissipated by exponential profiles having $R^2 > 0.9$ (see supporting information D for more details including a map of R^2). At these locations, K_ρ typically reaches $10^{-4} - 10^{-3}$ m^2 s^{-1}, in agreement with in situ observations above rough bathymetry [*Polzin et al*., 1997; *Kunze et al*., 2006; *Whalen et al*., 2012; *Klymak et al*., 2006]. Lower percentiles, though still exponential on average, continuously deform and end up resembling more and more a hump profile.

The map of the exponential decay scale z_0^* is reported in Figure 6a. Exponential profiles (brown to blue) clearly coincide with regions of high dissipation (hotspots of q). This is expected since exponential decay corresponds to large bottom amplitudes and hence, from equation (8), to large values of q (larger than $87\{1 - \exp[-4(0.4 - 0.1)]\} \sim 60\%$). The decay scale is typically smaller than 1000 m (80% of the dissipation). The lower decay scales (250–750 m) are found over regions exhibiting the strongest energy flux into internal tides, such as mid-ocean ridges. The same behavior was reported in *Melet et al*. [2013a], although the decay scale was for algebraically decaying dissipation profiles, based on the analytical model developed by P09 where internal tide dissipation is due to nonlinear wave-wave interactions. Regions near Iceland feature $z_0^* < 250$ m, though very large amplitudes due to poor tidal data give us little confidence in these results. Note that this decay scale is an e-folding value in the WKB-scaled vertical height z^*. Profiles in z coordinate are found to correlate more weakly with exponential decay (see supporting information D).

The spatial distribution of z_0^* can also be reasonably well understood from the bottom amplitude $A^{\mathrm{rms}}(0)$. Physically, larger bottom amplitudes yield faster decay, and we indeed find that $(1/z_0^*)^2$ scales quasi-linearly with $A^{\mathrm{rms}}(0)$. We propose the approximation

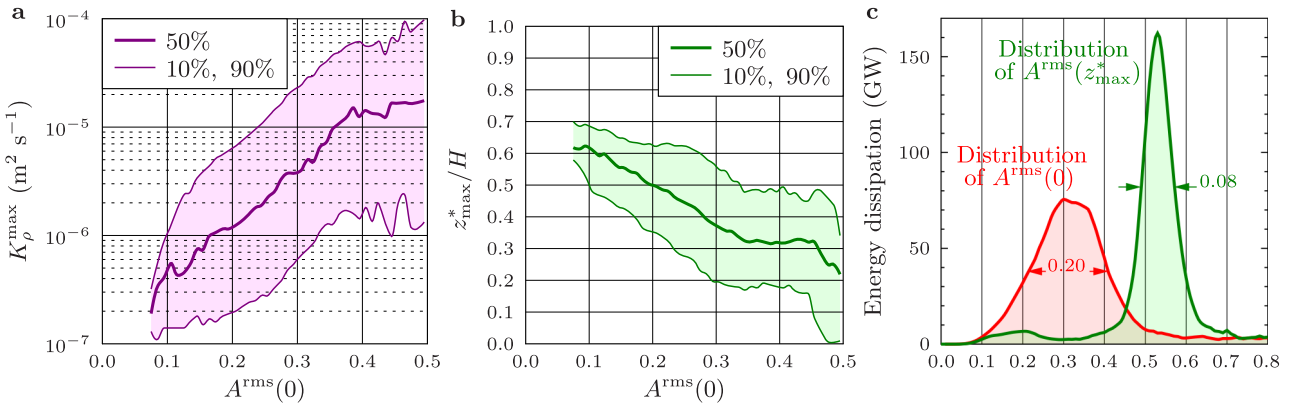

Figure 7. Quantitative characteristics of the hump profiles. (a) Maximum middepth diapycnal diffusivity $K_\rho(z^*_{\max})$. Note the quasi-exponential increase with the linear measure of bottom wave instability $A^{\rm rms}(0)$. (b) Corresponding relative height $z^*_{\max}/H$ decreasing with $A^{\rm rms}(0)$. In Figures 7a and 7b, the distribution is represented by the median (50%) and two extreme percentiles (10% and 90%). (c) Distribution of energy dissipation with respect to $A^{\rm rms}$ at $z^*=0$ and $z^*_{\max}$ (both integrals yield 20 GW). The distribution of $A^{\rm rms}(0)$ is the same as in Figure 5a. Note the half-maximum width change, suggesting that the criterion $A^{\rm rms}(z^*_{\max})\sim 0.5$ is sharper to determine $z^*_{\max}$.

$$z_0^{*\,\rm approx}=\frac{440}{\sqrt{A^{\rm rms}(0)-0.3}}, \tag{10}$$

(this expression is only formally valid for $A^{\rm rms}(0)>0.3$, which corresponds to the amplitude range for exponential profiles, see Figure 5a). Figure 6b shows that this expression recovers most of the salient features observed in Figure 6a, and excellent energetic agreement is found (supporting information D).

4.3.2. Hump Profiles

The analysis of the hump profiles (Figure 5b) reveals that the most energetic percentiles 80−95 exhibit a prominent middepth diffusivity maximum at $z^*_{\max}/H\sim 0.3-0.5$, which can be larger than the oceanic background value 10^{-5} m^2 s^{-1}. It is caused by an increased ambient stratification, not compensated by the WKB and $1/N^2$ scalings. Although the stratification at these locations is not stronger than elsewhere, the gradual increase of the buoyancy frequency $N(z)$ in the abyssal ocean suffices to make these waves, stable at the bottom, break well above the seafloor by decreasing their vertical lengthscale and increasing their amplitude (more details in section 3.3). This mechanism may substantiate the existing observations of nonmonotonic diffusivity profiles in various regions [*Toole et al.*, 1994; *Polzin et al.*, 1997; *Kunze et al.*, 2006; *Whalen et al.*, 2012; *Waterhouse et al.*, 2014].

As before, we seek relations between the characteristics of those profiles, namely the height and strength of the middepth maximum, and $A^{\rm rms}(0)$. In the analysis of hump profiles, we determine midlevel maximum values $K_\rho(z^*_{\max})$ as follows. We start at $z=0$ and list all points that are local maxima in the 300 m neighborhood above them. We then reject the "artificial" ones occurring in a 300 m neighborhood of the global maximum of N (thermocline) and select the one having the greatest K_ρ value. As seen in Figure 5b, only the most energetic profiles were found to possess such a maximum (indicated by a red dot), and Figures 7a and 7b only deal with those profiles.

The maximum diffusivity $K_\rho(z^*_{\max})$ increases with the bottom amplitude (Figure 7a), and its median value exceeds 10^{-5} m^2 s^{-1} for $A^{\rm rms}(0)>0.35$. The relative height $z^*_{\max}/H$ at which the maximum occurs is found to decrease with $A^{\rm rms}(0)$ (Figure 7b), which is consistent with the idea that more unstable bottom waves break at lower heights, being more sensitive to the increase of $N(z)$.

However, the height of maximum dissipation cannot be determined precisely from the relationship between $A^{\rm rms}(0)$ and $z^*_{\max}/H$. To determine a priori the height of the diffusivity maximum, we refine the previous analysis by looking at the would-be amplitude at the height where the maximum occurs $A^{\rm rms}(z^*_{\max})$, computed by the WKB theory as

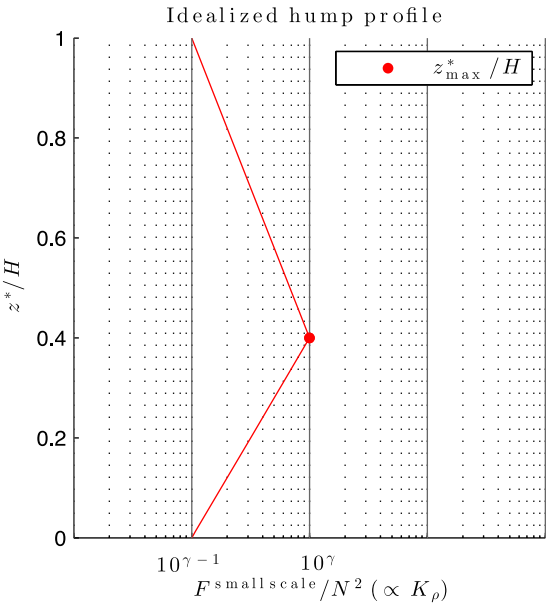

Figure 8. Idealized vertical profile of dissipation $F^{\text{small scale}}/N^2$ for hump profiles (note the WKB-scaled vertical coordinate z^*).

$$A^{\text{rms}}(z^*_{\text{max}}) = A^{\text{rms}}(0) \times \left(\frac{N^2(z^*_{\text{max}}) - \omega^2}{N^2(0) - \omega^2}\right)^{1/4}. \quad (11)$$

(Where no maximum is found, $A^{\text{rms}}(z^*_{\text{max}})$ is replaced by $A^{\text{rms}}(0)$ in Figure 7c. This gives rise to the slight bump around $A^{\text{rms}}(z^*_{\text{max}}) = 0.2$ and confirms that the points with a mid-water maximum account for the vast majority of energy dissipation.) Despite ignoring the nonlinear saturation that A undergoes between $z^* = 0$ and $z^* = z^*_{\text{max}}$, Figure 7c demonstrates that $A^{\text{rms}}(z^*_{\text{max}}) \sim 0.5$ may serve as a reasonable rule of thumb to determine a priori the height of the diffusivity maximum.

5. Implications for Tidal Dissipation Parameterizations

Some recent climate models account for tidal dissipation at large-scale bathymetry, parameterized by equation (1) [*St. Laurent et al.*, 2002], which we rewrite here with superscripts "large scale" to distinguish from the small-scale contribution:

$$\epsilon^{\text{large scale}}(x, y, z) \equiv q^{\text{large scale}}\, E_0^{\text{large scale}}(x, y)\, F^{\text{large scale}}(z). \quad (12)$$

As mentioned in section 1, in this paper, large-scale bathymetry refers to bathymetry resolved by satellite observations (*Smith and Sandwell* [1997], horizontal scales larger than $O(10$ km), while small-scale bathymetry refers to the unresolved scales, which are only known statistically [*Goff and Arbic*, 2010]. $E_0^{\text{large scale}}$ ($\sim$1 TW) is the bottom energy flux into internal tides radiated at large-scale bathymetry, the fraction of local dissipation $q^{\text{large scale}}$ is typically set to 30%, and the vertical profile $F^{\text{large scale}}(z)$ is typically assumed to decay exponentially with a decay scale of 500 m [*St. Laurent and Nash*, 2004]. The corresponding diapycnal diffusivity is given by $K_\rho = \Gamma\epsilon/N^2$ [*Osborn and Cox*, 1972], with a mixing efficiency $\Gamma = 0.2$.

To this, large-scale tidal dissipation should be added the contribution from small-scale waves, which we can parameterize similarly as

$$\epsilon^{\text{small scale}}(x, y, z) \equiv q^{\text{small scale}}(x, y)\, E_0^{\text{small scale}}(x, y)\, F^{\text{small scale}}(x, y, z). \quad (13)$$

We have shown that the inhomogeneous distribution of the fraction of local dissipation $q^{\text{small scale}}$ and the vertical dissipation profile $F^{\text{small scale}}$ can both be captured by a single theoretical measure of the bottom linear wave amplitude $A^{\text{rms}}(0)$ given in equation (7). $A^{\text{rms}}(0)$ is a function of the abyssal hill bathymetry, the tidal forcing, and the bottom stratification. Technically, the modeled bottom and vertical profile of stratification is the only evolving field required as input for the analytical model presented in this study to determine the time-evolving 3-D distribution of abyssal-hill radiated internal-tide dissipation. Evolving bathymetry and tidal forcing are also natural inputs for our model in paleoclimate applications.

Specifically, $q^{\text{small scale}}$ is given by the approximate relationship equation (8). $F^{\text{small scale}}$ corresponds to N^2 times exponential decay if $A^{\text{rms}}(0) \geq 0.4$, and to N^2 times a hump profile if $A^{\text{rms}}(0) < 0.4$.

Exponential profiles $F^{\text{small scale}}(z^*)/N^2 \propto \mathrm{e}^{-z^*/z^*_0}$ have a decay scale given by equation (10) (in WKB-scaled vertical height z^*, equation (9)). As in the large-scale parameterization equation (12), $F^{\text{small scale}}$ is normalized such that $\int_0^H F^{\text{small scale}}(z)\, dz = 1$, where $H(x, y)$ is the local ocean depth.

Given the small diffusivities associated with hump profiles (Figure 5b), one possibility would be to simply ignore them, especially those with $A^{\text{rms}}(0) < 0.3$. But collectively, these small contributions add up to a non-negligible dissipation (Figure 5a), and it may be desirable to account for them. Based on Figure 5b, we propose the following idealized profile for $F^{\text{small scale}}/N^2 \propto K_\rho$ (Figure 8): $\log_{10}(F^{\text{small scale}}(z^*)/N^2)$ piecewise

linear, increasing from $\gamma-1$ to γ at z^*_{max}, and decreasing back to $\gamma-1$ at H. From Figure 7c, z^*_{max} is determined by $A^{rms}(z^*_{max})=0.5$, where $A^{rms}(z^*)$ is given by equation (11). Finally, the value of γ is determined by applying the energetic constraint $\int_0^H F^{small\ scale}(z)\,dz=1$.

6. Conclusions and Discussion

Breaking internal tides are thought to provide a large part of the power needed to mix the abyssal ocean and sustain the meridional overturning circulation. Despite the importance of internal-tide-driven mixing for the ocean state, its spatial distribution remains poorly quantified. In the present study, we focus on the dissipation of the principal lunar semidiurnal (M_2) internal tides generated at small-scale abyssal hills, which dominate the seafloor topography at scales smaller than O(10 km). We provide a first worldwide estimate of the fraction of energy that these waves lose locally, close to their generation site, due to convective instabilities (density overturning), and of the associated vertical profile of dissipation. Our estimates are based on an analytical model relying on linear wave theory and an ad hoc parameterization for wave breaking called wave saturation. This simple and cost-efficient tool is first tested regionally over the mid-Atlantic ridge where observations of internal-tide energy dissipation are available, and then applied globally using statistical distributions of quasi-global small-scale abyssal hill bathymetry, stratification and M_2 tidal velocities.

Our results suggest that tidal mixing from abyssal hills is highly inhomogeneous, both horizontally and vertically. A large fraction of abyssal-hill generated internal-tide energy is dissipated locally (60–90%) over large parts of the mid-Atlantic ridge, the central Indian ridge, and the East Pacific rise, where abyssal hills are responsible for large barotropic to internal tide energy conversion. Globally, the dissipation amounts to about 60% of the 0.1 TW of internal tides generated at abyssal hills. If the local energy dissipation is compared to the energy converted from the barotropic to internal tides by all scales of bathymetry (not only abyssal hills), then the fraction of local dissipation of abyssal-hill generated internal tides is still dominated by the mid-ocean ridges of the Southern Hemisphere, but its magnitude is lowered to 20–60%.

The diapycnal diffusivity induced by M_2 internal tides generated at abyssal hills follows two different types of vertical profiles: the widely used exponential decay, responsible for most of the dissipation, and a novel hump profile with middepth maxima. Exponentially decaying profiles dominate limited areas of strong energy flux into internal tides and the corresponding vertical decay scale varies with space. Hump profiles dominate larger areas of less energetic, more stable bottom waves, which break and dissipate well above the seafloor as a result of increasing ocean stratification.

The heterogeneity of the mixing that this work points out could have important implications for the ocean state, which has been shown to be significantly impacted by both the horizontal and vertical distributions of diapycnal mixing. The Southern Hemisphere seems to present favorable conditions for particularly high mixing rates due to abyssal-hill generated internal tides. Given the central role of the Southern Ocean in ventilating deep water masses [*Jayne*, 2009; *Talley*, 2013], the spatial distribution of mixing suggested by our study could impact the ocean circulation and water mass transformation in the deep ocean. A recent estimate indeed shows that 25% of the transformation of Antarctic Bottom Water driven by local internal-tide mixing is attributed to internal tides generated at abyssal hills (C. de Lavergne et al., On the consumption of Antarctic Bottom Water in the abyssal ocean, submitted to *Journal of Physical Oceanography*, 2015).

The potential implementation of a parameterization of internal-tide-driven mixing above abyssal hills has also been presented in this study. The fraction of local dissipation and the vertical profile of dissipation can be related to a linear wave amplitude at the seafloor through simple empirical relationships. The corresponding parameterization would allow the mixing to evolve in time as it depends on the stratification simulated by the model, on static geological properties (abyssal hill bathymetry) and on the barotropic tidal velocities.

Unlike observations and numerical simulations, the simplicity of the wave saturation method makes it possible to derive a global map of tidal dissipation at abyssal hills. However, the simplifying assumptions that go into this model imply important limitations. First, the generation of internal tides uses linear subcritical theory, whose validity is thought to extend beyond the formal limit of low bathymetric slopes [*Garrett and Kunze*, 2007]. An empirical correction has however been applied to remove the smallest scales responsible

for supercritical slopes. About half of the area covered by abyssal hills is found to be supercritical, and the correction reduces the average bottom amplitude of the waves by 30%. But energetically, the global tidal conversion is only reduced by 3%. This is because without the supercriticality correction, the amplitude of some of the smallest scale waves is overestimated. These break at or very close to the seafloor, without altering the global picture, and overall our dissipation estimates are not strongly affected by this correction. This being said, the correction is empirical, and it cannot be ruled out that a more accurate treatment of supercriticality could impact our results more strongly. Second, the theory assumes a semiinfinite ocean, neglecting the reflection of the waves reaching the ocean surface back into the interior and their potential interaction with upward-propagating waves. The waves that propagate away beyond one surface reflection are assumed to be dissipated nonlocally and to contribute to the background oceanic diffusivity $O(10^{-5}\ \mathrm{m^2\ s^{-1}})$. Additional uncertainties arise from the use of the WKB approximation (especially near the thermocline when stratification variations can be large), from the statistical approach and geological parameters used to represent abyssal hills, and from the ad hoc wave saturation scheme. The choice of parameters that go into this scheme, such as the spatial domain length, resolution (both horizontal and vertical), saturation threshold and "impact length" all influence our results to various degrees. A sensitivity analysis of the global dissipation fraction (found to be around 60%) has been conducted, and shows reasonable robustness to those parameters (dissipation always in the range 55–65%), with greatest sensitivity to spatial resolution (see supporting information C). Although our regional study shows that wave saturation predicts the observed dissipation profile in the Brazil Basin, the global validity of this simple analytical tool needs to be assessed. In particular, it does not take into account the contribution from instabilities due to nonlinear wave-wave interactions and topographic scattering. Quantitatively, our estimates are thus likely below actual dissipation rates. But qualitatively, we believe that the inhomogeneity of the 3-D tidal dissipation and mixing that this work suggests and its enhancement over mid-ocean ridges of the Southern Hemisphere are robust. Finally, a major limitation is that we only investigate abyssal-hill generated internal tides. The fine resolution required to satisfactorily resolve the small scales of the abyssal hill spectrum prevents us from accounting for both the large-scale bathymetry from satellite measurements and the abyssal hills (the former requiring large computational domains). We believe that including the large-scale bathymetry in future computations would constitute an improvement and enable to assess its contribution to the spatial inhomogeneity of tidal dissipation, both horizontally and vertically.

Acknowledgments

The data used in this study are available upon request from the authors (lefauve@damtp.cam.ac.uk). A.L. and C.M. gratefully acknowledge financial support from the Chair for Sustainable Development at Ecole Polytechnique. The authors would like to thank M. Nikurashin for useful discussions about this work and helpful comments that lead to improvements in the manuscript. We also thank S. Falahat for providing us with the stratification data and A. Goff and B. Arbic for the abyssal hills spectrum data. Finally, the authors would like to thank the anonymous reviewers for their valuable comments.

References

Alford, M. H., et al. (2011), Energy flux and dissipation in Luzon strait: Two tales of two ridges, *J. Phys. Oceanogr.*, *41*(11), 2211–2222.

Althaus, A. M., E. Kunze, and T. B. Sanford (2003), Internal tide radiation from mendocino escarpment, *J. Phys. Oceanogr.*, *33*, 1510–1527.

Balmforth, N. J., and T. Peacock (2009), Tidal conversion by supercritical topography, *J. Phys. Oceanogr.*, *39*(8), 1965–1974.

Bell, T. H. (1975a), Lee waves in stratified flows with simple harmonic time dependence, *J. Fluid Mech.*, *67*, 705–722.

Bell, T. H. (1975b), Topographically generated internal waves in the open ocean, *J. Geophys. Res.*, *80*, 320–327.

Bühler, O., and C. J. Muller (2007), Instability and focusing of internal tides in the deep ocean, *J. Fluid Mech.*, *588*, 1–28.

Canuto, V. M., A. M. Howard, Y. Cheng, C. J. Muller, A. Leboissetier, and S. R. Jayne (2010), Ocean turbulence, III: New GISS vertical mixing scheme, *Ocean Modell.*, *34*, 70–91.

Carter, G. S., M. A. Merrifield, J. M. Becker, K. Katsumata, M. C. Gregg, D. S. Luther, M. D. Levine, T. J. Boyd, and Y. L. Firing (2008), Energetics of M_2 barotropic to-baroclinic tidal conversion at the Hawaiian islands, *J. Phys. Oceanogr.*, *38*, 2205–2223.

Charette, M. A., and W. H. F. Smith (2010), The volume of the Earths ocean, *Oceanography*, *23*(2), 112–114.

Egbert, G. D., and S. Y. Erofeeva (2002), Efficient inverse modeling of barotropic ocean tides, *J. Atmos. Oceanic Technol.*, *19*, 183–204.

Egbert, G. D., and R. D. Ray (2000), Significant dissipation of tidal energy in the deep ocean inferred from satellite altimeter data, *Nature*, *405*, 775–778.

Falahat, S., J. Nycander, F. Roquet, and M. Zarroug (2014), Global calculation of tidal energy conversion into vertical normal modes, *J. Phys. Oceanogr.*, *44*, 3225–3244.

Flato, G., et al. (2013), Evaluation of climate models, in *Climate Change 2013: The Physical Science Basis. Contribution of Working Group I to the Fifth Assessment Report of the Intergovernmental Panel on Climate Change*, chap. 9, pp. 741–866, Cambridge Univ. Press, Cambridge, U. K.

Garrett, C., and E. Kunze (2007), Internal tide generation in the deep ocean, *Annu. Rev. Fluid Mech.*, *39*, 57–87.

Gill, A. E. (1982), *Atmosphere-Ocean Dynamics*, vol. 30, Academic, San Diego, Calif.

Goff, J. A., and B. K. Arbic (2010), Global prediction of abyssal hill roughness statistics for use in ocean models from digital maps of paleo-spreading rate, paleo-ridge orientation, and sediment thickness, *Ocean Modell.*, *32*(1), 36–43.

Goff, J. A., Y. Ma, A. Shah, J. R. Cochran, and J.-C. Sempéré (1996), Stochastic analysis of seafloor morphology on the flanks of the Southeast Indian Ridge: The influence of ridge morphology on the formation of abyssal hills, *J. Geophys. Res.*, *102*, 15,521–15,534.

Jayne, S. R. (2009), The impact of abyssal mixing parameterizations in an ocean general circulation model, *J. Phys. Oceanogr.*, *39*(7), 1756–1775.

Khatiwala, S. (2003), Generation of internal tides in an ocean of finite depth: Analytical and numerical calculations, *Deep Sea Res., Part I*, *50*, 3–21.

Klymak, J. M., J. N. Moum, J. D. Nash, E. Kunze, J. B. Girton, G. S. Carter, C. M. Lee, T. B. Sanford, and M. C. Gregg (2006), An estimate of tidal energy lost to turbulence at the Hawaiian Ridge, *J. Phys. Oceanogr.*, *36*, 1148–1164.

Kunze, E., E. Firing, J. M. Hummon, T. K. Chereskin, and A. M. Thurnherr (2006), Global abyssal mixing inferred from lowered ADCP shear and CTD strain profiles, *J. Phys. Oceanogr.*, *36*(8), 1553–1576.
Ledwell, J. R., E. T. Montgomery, K. L. Polzin, L. C. St. Laurent, R. W. Schmitt, and J. M. Toole (2000), Evidence for enhanced mixing over rough topography in the abyssal ocean, *Nature*, *403*, 179–182.
Llewellyn Smith, S. G., and W. R. Young (2002), Conversion of the Barotropic Tide, *J. Phys. Oceanogr.*, *32*, 1554–1566.
Macdonald, K. C., P. J. Fox, R. T. Alexander, R. Pockalny, and P. Gente (1996), Volcanic growth faults and the origin of pacific abyssal hills, *Nature*, *380*, 125–129.
McDougall, T. J., and P. M. Barker (2011), Getting started with TEOS–10 and the Gibbs Seawater (GSW) Oceanographic Toolbox, 28 pp., SCOR/IAPSO WG127. [Available at www.teos-10.org.]
Melet, A., R. Hallberg, S. Legg, and K. Polzin (2013a), Sensitivity of the ocean state to the vertical distribution of internal-tide-driven mixing, *J. Phys. Oceanogr.*, *43*(3), 602–615.
Melet, A., M. Nikurashin, C. Muller, S. Falahat, J. Nycander, P. G. Timko, B. K. Arbic, and J. A. Goff (2013b), Internal tide generation by abyssal hills using analytical theory, *J. Geophys. Res. Oceans*, *118*, 6303–6318, doi:10.1002/2013JC009212.
Melet, A., R. Hallberg, S. Legg, and M. Nikurashin (2014), Sensitivity of the ocean state to lee wave-driven mixing, *J. Phys. Oceanogr.*, *44*(3), 900–921.
Muller, C. J., and O. Bühler (2009), Saturation of the internal tides and induced mixing in the abyssal ocean, *J. Phys. Oceanogr.*, *39*, 2077–2096.
Munday, D. R., L. C. Allison, H. L. Johnson, and D. P. Marshall (2011), Remote forcing of the Antarctic circumpolar current by diapycnal mixing, *Geophys. Res. Lett.*, *38*, L08609, doi:10.1029/2011GL046849.
Munk, W., and C. Wunsch (1998), Abyssal recipes II: Energetics of tidal and wind mixing, *Deep Sea Res., Part I*, *45*, 1977–2010.
Nikurashin, M., and S. Legg (2011), A mechanism for local dissipation of internal tides generated at rough topography, *J. Phys. Oceanogr.*, *41*(2), 378–395.
Nikurashin, M., and G. Vallis (2012), A theory of the interhemispheric meridional overturning circulation and associated stratification, *J. Phys. Oceanogr.*, *42*(10), 1652–1667.
Niwa, Y., and T. Hibiya (2004), Three-dimensional numerical simulation of M_2 internal tides in the east China Sea, *J. Geophys. Res.*, *109*, C04027, doi:10.1029/2003JC001923.
Nycander, J. (2006), Tidal generation of internal waves from a periodic array of steep ridges, *J. Fluid Mech.*, *567*, 415–432.
Osborn, T., and C. Cox (1972), Oceanic fine structure, *Geophys. Astrophys. Fluid Dyn.*, *3*, 321–345.
Polzin, K. L. (2004), A heuristic description of internal wave dynamics, *J. Phys. Oceanogr.*, *34*(1), 214–230.
Polzin, K. L. (2009), An abyssal recipe, *Ocean Modell.*, *30*(4), 298–309.
Polzin, K. L., J. M. Toole, and R. W. Schmitt (1995), Finescale parameterizations of turbulent dissipation, *J. Phys. Oceanogr.*, *25*(3), 306–328.
Polzin, K. L., J. M. Toole, J. R. Ledwell, and R. W. Schmitt (1997), Spatial variability of turbulent mixing in the abyssal ocean, *Science*, *276*(5309), 93–96.
Saenko, O. A., and W. J. Merryfield (2005), On the effect of topographically enhanced mixing on the global ocean circulation, *J. Phys. Oceanogr.*, *35*, 826–834.
Samelson, R. M. (1998), Large-scale circulation with locally enhanced vertical mixing, *J. Phys. Oceanogr.*, *28*(4), 712–726.
Sheen, K. L., et al. (2013), Rates and mechanisms of turbulent dissipation and mixing in the southern ocean: Results from the diapycnal and isopycnal mixing experiment in the southern ocean (dimes), *J. Phys. Oceanogr.*, *118*, 2774–2792.
Simmons, H. L., S. R. Jayne, L. C. St. Laurent, A. J. Weaver (2004), Tidally driven mixing in a numerical model of the ocean general circulation, *Ocean Modell.*, *6*, 245–263.
Smith, W. H. F., and D. T. Sandwell (1997), Global sea floor topography from satellite altimetry and ship depth soundings, *Science*, *277*, 1956–1962.
St. Laurent, L. C., and C. Garrett (2002), The role of internal tides in mixing the deep ocean, *J. Phys. Oceanogr.*, *32*, 2882–2899.
St. Laurent, L. C., and J. D. Nash (2004), An examination of the radiative and dissipative properties of deep ocean internal tides, *Deep Sea Res., Part II*, *51*(25), 3029–3042.
St. Laurent, L. C., H. L. Simmons, and S. R. Jayne (2002), Estimating tidally driven mixing in the deep ocean, *Geophys. Res. Lett.*, *29*(23), 2106, doi:10.1029/2002GL015633.
Staquet, C., and J. Sommeria (2002), Internal gravity waves: From instabilities to turbulence, *Annu. Rev. Fluid Mech.*, *34*(1), 559–593.
Sutherland, B. (2010), *Internal Gravity Waves*, Cambridge Univ. Press, Cambridge, U. K.
Talley, L. D. (2013), Closure of the global overturning circulation through the Indian, Pacific, and Southern Oceans: Schematics and transports, *Oceanography*, *26*(1), 80–97.
Thurnherr, A. M., and L. C. St. Laurent (2011), Turbulence and diapycnal mixing over the east pacific rise crest near 108n, *Geophys. Res. Lett.*, *38*, L15613, doi:10.1029/2011GL048207.
Toole, J., R. W. Schmitt, and K. L. Polzin (1994), Estimates of diapycnal mixing in the abyssal ocean, *Science*, *264*, 1120–1123.
Waterhouse, A. F., et al. (2014), Global patterns of diapycnal mixing from measurements of the turbulent dissipation rate, *J. Phys. Oceanogr.*, *44*, 1854–1872.
Waterman, S., A. C. N. Garabato, and K. L. Polzin (2013), Internal waves and turbulence in the Antarctic circumpolar current, *J. Phys. Oceanogr.*, *43*, 259–282.
Whalen, C. B., L. D. Talley, and J. A. MacKinnon (2012), Spatial and temporal variability of global ocean mixing inferred from Argo profiles, *Geophys. Res. Lett.*, *39*, L18612, doi:10.1029/2012GL053196.
Wunsch, C. (2000), Moon, tides and climate, *Nature*, *405*, 743–744.
Wunsch, C., and R. Ferrari (2004), Vertical mixing, energy, and the general circulation of the oceans, *Annu. Rev. Fluid Mech.*, *36*(1), 281–314, doi:10.1146/annurev.fluid.36.050802.122121.
Zhao, Z., M. H. Alford, and J. B. Girton (2012), Mapping low-mode internal tides from multisatellite altimetry, *Oceanography*, *25*(2), 42–51.
Zilberman, N. V., J. M. Becker, M. A. Merrifield, and G. S. Carter (2009), Model estimates of M_2 internal tide generated over mid-Atlantic ridge topography, *J. Phys. Oceanogr.*, *39*, 2635–2651.